PAPER

Check for updates

Self-supported Co₃O₄@Zn–CoNi₂S₄/NF core–shell nanoarrays as an efficient bifunctional electrode for overall water splitting

Xuan Zhao,[a] Yu Dong,[a] Zhijie Wang,[a] Yusheng Qiu,[a] Ende Wang,[b] Naikun Sun[*a] and Yongli Tong [ID] [*a]

It is a crucial matter to develop bifunctional transition metal catalysts for water electrolysis. In this study, we fabricate a Co₃O₄@Zn–CoNi₂S₄ core–shell heterostructure supported on nickel foam (Co₃O₄@Zn–CoNi₂S₄/NF). The compound structure can generate more active centers and exhibit some unique characteristics. Moreover, the doping of Zn further enhances the catalytic performance. It can optimize the lattice structure of the Co₃O₄@CoNi₂S₄/NF heterostructure and reduce the reaction energy barrier effectively, which can meet the relatively strict requirements of high-performance electrocatalysts. This material can be used as an efficient bifunctional electrocatalyst. In 1 M KOH electrolyte, the material shows excellent electrocatalytic performance for OER and HER. It possesses a low overpotential of 190 mV at 10 mA cm⁻² for OER and 120 mV at 10 mA cm⁻² for HER. Also, it maintains long-term stability. The Co₃O₄@Zn–CoNi₂S₄/NF electrolytic cell acts as a two-electrode system for overall water splitting. It needs a battery voltage of 1.45 V to drive the current density to 10 mA cm⁻². This research has proved that combining metal doping with heterogeneous interface design is a feasible strategy for developing high-performance bifunctional electrocatalysts.

1 Introduction

Addressing the severe global energy shortage and environmental deterioration necessitates the pursuit of highly efficient hydrogen production strategies.[1,2] Hydrogen is a highly promising energy carrier because of its large storage capacity, wide – ranging applicability, and natural sustainability. Among the available hydrogen production techniques, electrochemical water splitting has become a focal point of research. This is mainly because it is technologically well – developed, easy to operate, and highly efficient.[3,4] Electrochemical water splitting is based on two fundamental half – reactions. At the cathode, the hydrogen evolution reaction (HER) occurs, while at the anode, the oxygen evolution reaction (OER) takes place. These two reactions are the core of the water electrolysis process for hydrogen production. During the HER at the cathode, breaking down H_2O to obtain H demands overcoming a relatively high energy threshold.[5–8] Meanwhile, the OER at the anode involves a complex four – electron transfer mechanism with slow reaction kinetics. This slow kinetics acts as a limiting factor, reducing the overall efficiency of water splitting. Moreover, conventional electrode materials typically have low catalytic

capabilities. In severe alkaline conditions, they are susceptible to corrosion and the detachment of active substances, which causes a rapid decline in performance.[9,10] These problems lead to the degradation of catalytic performance. Therefore, developing catalysts with three key capabilities has become a current research focus.[11]

Among various potential materials, cobalt oxide (Co_3O_4) has distinguished itself as a superior candidate for designing stable and bifunctional electrocatalysts.[12–14] Co_3O_4 is a multi-valence source. The Co^{2+} sites offer abundant active sites for electron transfer and reactant adsorption. Its mixed-valences source offers a rich range of active sites to transfer electrons. In OER Co ions interact stably with oxygenate species and have good reaction kinetics. However, the electrocatalytic performance of Co_3O_4 is severely degraded by poor electrical conductivity and low catalytic activity.[15] During the HER, Co^{3+} sites in Co_3O_4 strongly bind hydrogen intermediates (H), impeding H_2 formation. Furthermore, their reduction to Co^{2+} under cathodic potential stabilizes OH^- adsorption, generating Co–OH species that block the remaining active sites, thus further poisoning the HER activity.[16–19] To solve these difficulties and improve the electrochemical performance of Co_3O_4 materials, researchers have fabricated a composite material using complementary substances such as metals, semiconductors, other oxides and sulfides.[20–22] Transition metal sulfides like $CoNi_2S_4$ are particularly attractive as they provide metallic conductivity, a rich number of redox couples (Co^{2+}/Co^{3+}, Ni^{2+}/Ni^{3+}) of charge

aSchool of Science, Shenyang Ligong University, Shenyang 110159, P. R. China. E-mail: naikunsun@163.com; tyl.tongyongli@163.com

bSchool of Equipment Engineering, Shenyang Ligong University, Shenyang 110159, P. R. China

transport. The incorporation of sulfides introduces sulfur vacancies, which not only increase carrier concentration but also expand the electrochemically active surface area.[23–25] Zheng et al. demonstrated that a $Ni(OH)_2@NiCo_2S_4$ composite exhibiting a low overpotential of 230 mV at 20 mA cm^{-2} under alkaline conditions. This superior performance was ascribed to the improved charge transport facilitated by the conductive sulfide scaffold.[26]

However, Relying merely on the simple composite of two materials, the interface regulation methods are relatively singular, making it difficult to achieve precise control over the interfacial electronic structure and active sites.[27,28] In order to realize improved control over intrinsic activity, heteroatom doping is adopted. For example, zinc (Zn), possessing a stable fully filled configuration, serves as an ideal dopant to regulate the electron density of the host lattice without introducing competing redox active sites.[29,30] These characteristics enable effective regulation of the electron distribution in the support or host material. Additionally, Zn^{2+} possesses a large ionic radius. When doped into the lattice, it readily induces significant lattice distortion.[31] Consequently, these combined characteristics offer a novel strategy for engineering highly efficient bifunctional electrocatalysts.

Herein, we systematically investigate the impact of Zn doping on $Co_3O_4@CoNi_2S_4$/NF by constructing a core–shell heterostructure $Co_3O_4@Zn–CoNi_2S_4$/NF electrocatalyst via a facile hydrothermal strategy followed by thermal annealing. With the introduction of the $CoNi_2S_4$ precursor, $CoNi_2S_4$ nanosheets were in situ grown on Co_3O_4 nanowires. This structural design provides more free electrons and a larger specific surface area for the catalytic reaction process. Meanwhile, Zn doping induces structural evolution and lattice modulation of the $Co_3O_4@CoNi_2S_4$ composite, which helps expose additional active sites. Electrochemical tests were conducted in an electrolyte of 1 M KOH. For the OER, the overpotential of the prepared catalyst at a current density of 10 mA cm^{-2} was 190 mV, which was 113 mV lower than that of the Co_3O_4/NF catalyst. In the HER test, the overpotential of this catalyst corresponding to a current density of 10 mA cm^{-2} was 119 mV. In addition, when used as both the cathode and anode for bifunctional water electrolysis, $Co_3O_4@Zn–CoNi_2S_4$/NF exhibited excellent performance. It only required a cell voltage of 1.45 V to reach a current density of 10 mA cm^{-2}.

2 Experimental

2.1 Materials preparation

2.1.1. Preparation of Co_3O_4/NF. The Co_3O_4/NF sample was prepared by a one-step hydrothermal method. Firstly, 0.582 g of $Co(NO_3)_2 \cdot 6H_2O$, 0.07 g of NH_4F, 0.6 g of $CO(NH_2)_2$, and 60 mL of deionized water (DI) were mixed and stirred thoroughly until completely dissolved, followed by immersing nickel foam (NF) in the solution. The prepared solution was transferred into a 100 mL Teflon-lined autoclave and heated at 120 °C for 8 h. The Co_3O_4/NF precursor was obtained, which was repeatedly washed with C_2H_5OH and DI water, then dried at 60 °C for 7 h. Subsequently, the precursor was calcined in a muffle furnace at

a heating rate of 2 °C min^{-1}, raised to 350 °C, and held at that temperature for 2 h. Finally, Co_3O_4/NF was obtained.

2.1.2. Preparation of $Co_3O_4@CoNi_2S_4$/NF. To fabricate the $Co_3O_4@CoNi_2S_4$/NF heterostructure, a secondary hydrothermal treatment was employed. Specifically, 0.582 g of $Co(NO_3)_2 \cdot 6H_2O$, 0.2908 g $Ni(NO_3)_2 \cdot 6H_2O$ and 0.2 g of Na_2S were dissolved in 60 mL of DI water under vigorous magnetic stirring. The previously calcined Co_3O_4/NF substrate was immersed in this solution within a Teflon-lined autoclave. The system was heated at 120 °C for 8 h and then allowed to cool naturally. The final product, denoted as $Co_3O_4@CoNi_2S_4$/NF, was washed and dried in an oven for 7 h.

2.1.3. Preparation of $Co_3O_4@Zn–CoNi_2S_4$/NF. The synthesis protocol for $Co_3O_4@Zn–CoNi_2S_4$/NF mirrors that of $Co_3O_4@CoNi_2S_4$/NF, with the modification of introducing an additional 0.06 g of $Zn(NO_3)_2 \cdot 6H_2O$ during the precursor solution preparation. The subsequent hydrothermal and drying procedures remained identical to those described above.

Specifically, to investigate the effect of sulfide loading, precursor solutions with total metal ion concentrations of 0.025 M, 0.100 M, and 0.150 M were employed, maintaining a constant Co/Ni molar ratio of 1 : 2. These samples were labeled as C-25, C-100, and C-150, respectively. Additionally, to evaluate the impact of Zn incorporation, samples with varying Zn doping contents (nominal concentrations of 1, 5, and 6 at%) were prepared under otherwise identical conditions.

2.2 Material characterizations

The morphology of the catalysts was characterized using a scanning electron microscope (SEM, Model Quanta 450 FEG), a transmission electron microscope (TEM, Model JEM-2020 F), and an X-ray energy dispersive spectrometer (EDS, Model SUPER-X EDX). The Brunauer–Emmett–Teller (BET) surface area was determined using N_2 adsorption at 77 K. Electron paramagnetic resonance (EPR) spectroscopy was performed on a Bruker EMX-10/12 spectrometer at room temperature to detect unpaired electrons associated with oxygen vacancies. Meanwhile, the microstructure, crystallographic orientation, and elemental composition of the as-prepared nanoparticles were analyzed. The crystallographic structures of the catalysts were determined via an X-ray powder diffractometer (XRD, Model D8 Discovery). The surface chemical states and elemental valences of the catalysts were investigated using an X-ray photoelectron spectrometer (XPS, Model ESCALAB 250 Xi).

2.3 Electrochemical measurements

The electrochemical performance was evaluated in a standard three-electrode configuration using a CHI 760E workstation, with a 1.0 mol L^{-1} aqueous potassium hydroxide (KOH) solution as the electrolyte. The sample was used as the working electrode, the Pt sheet was used as the counter electrode (surface area 1 cm^2), and Hg/HgO was used as the reference electrode respectively. Linear Sweep Voltammetry (LSV) curves were recorded at a scan rate of 5 mV s^{-1} with 90% iR (ohmic) compensation. For the Oxygen Evolution Reaction (OER), a reverse scan was employed to minimize interference from the

oxidation peak of nickel species. The Tafel slope, a core parameter describing the relationship between the kinetic rate of the electrocatalytic reaction and the overpotential, was calculated from the polarization curves using the following equation:

$$\eta = a \log j + b$$

where η is the overpotential, b is the Tafel slope, j is the current density, and a is a constant.[27] Electrochemical Impedance Spectroscopy (EIS) measurements were conducted over a frequency range of 100 kHz to 0.1 Hz. The stability of the electrode was assessed *via* chronopotentiometry (CP). Additionally, the electrochemical double-layer capacitance (C_{dl}) was determined as follows: cyclic voltammetry tests were performed in the non-faradaic region at different scan rates ranging from 10 to 50 mV s^{-1}, and the C_{dl} value is represented by the slope of the plot of current density *versus* scan rate.

3 Results and discussion

3.1 Characterization analyses

The Co$_3$O$_4$@Zn–CoNi$_2$S$_4$/NF sample is fabricated *via* a two-step hydrothermal synthesis combined with heat treatment. The flow chart of the sample preparation mechanism is shown in Fig. 1. The synthesis begins with growing Co$_3$O$_4$ nanowires on the NF support *via* a hydrothermal method and calcination. These nanowires serve as a skeleton for the secondary growth of CoNi$_2$S$_4$ nanosheets. The resulting Co$_3$O$_4$@CoNi$_2$S$_4$/NF structure provides a larger specific surface area for subsequent doping. During the second hydrothermal synthesis, Zn^{2+} is introduced into the solution, leading to the successful preparation of the Co$_3$O$_4$@Zn–CoNi$_2$S$_4$/NF sample. The surface morphologies of the as-prepared Co$_3$O$_4$/NF, Co$_3$O$_4$@CoNi$_2$S$_4$/NF, and Co$_3$O$_4$@Zn–CoNi$_2$S$_4$/NF are examined by SEM. The corresponding SEM images are shown in Fig. 2a–c. In Fig. 2a, Co$_3$O$_4$/NF forms a nanowire array structure where the nanowires grow regularly on the NF substrate with a smooth surface. Fig. 2b displays the microstructure of Co$_3$O$_4$@CoNi$_2$S$_4$/NF. When CoNi$_2$S$_4$ is composited onto the surface of Co$_3$O$_4$/NF,

a nanosheet structure is *in situ* grown on the surface of the pristine Co$_3$O$_4$ nanowires. This unique structure provides a significantly larger surface area, which facilitates the following doping process. As shown in Fig. 2c, the Co$_3$O$_4$@Zn–CoNi$_2$S$_4$ sample maintains this morphology after Zn^{2+} doping. It exhibits a typical core–shell structure, where the inner nanowires are tightly wrapped by the outer nanosheets. As shown in Fig. S2, the isotherm is of typical Type IV with an H$_3$ hysteresis loop at $P/P_0 > 0.4$, indicative of a mesoporous structure formed by slit-like pores. The BET specific surface area is determined to be 43.34 m^2 g^{-1}, and the mesoporous nature is further verified by the pore size distribution. This large surface area and porous architecture not only expose abundant active sites but also promote electrolyte infiltration and ion diffusion, which are crucial for improving electrocatalytic activity. As illustrated in Fig. 2d, the TEM characterization results confirm that Co$_3$O$_4$@Zn–CoNi$_2$S$_4$/NF exhibits a micro-heterostructure, where nanosheets are tightly wrapped around the nanowire core, and this structural feature is clearly observable. HRTEM is used to further verify the heterostructure. As illustrated in Fig. 2e, well-defined lattice fringes are visualized. The interplanar distances of 0.47 nm and 0.24 nm are in excellent agreement with the (111) and (311) crystal planes of Co$_3$O$_4$, respectively. In contrast, the interplanar spacing of 0.27 nm is consistent with the (222) plane of CoNi$_2$S$_4$. Moreover, a clear heterophasic interface is detected between the lattice structures of Co$_3$O$_4$ and CoNi$_2$S$_4$. Such heterogeneous interfaces are capable of triggering spontaneous electron transfer across the interfacial regions, which in turn facilitates the optimization of electron transportation dynamics during the catalytic reactions occurring on the surface of Co$_3$O$_4$@Zn–CoNi$_2$S$_4$/NF.[32,33] Additionally, active sites situated near heterogeneous interfaces exhibit enhanced efficiency in adsorbing reactants, activating reaction intermediates, and reducing the energy barrier for chemical reactions.[34] The SAED pattern and corresponding EDS results are displayed in Fig. 2f and g. The SAED pattern shows typical polycrystalline diffraction ring characteristics. This further confirms that the sample has a composite crystalline structure. The phase composition matches the TEM data, confirming the formation
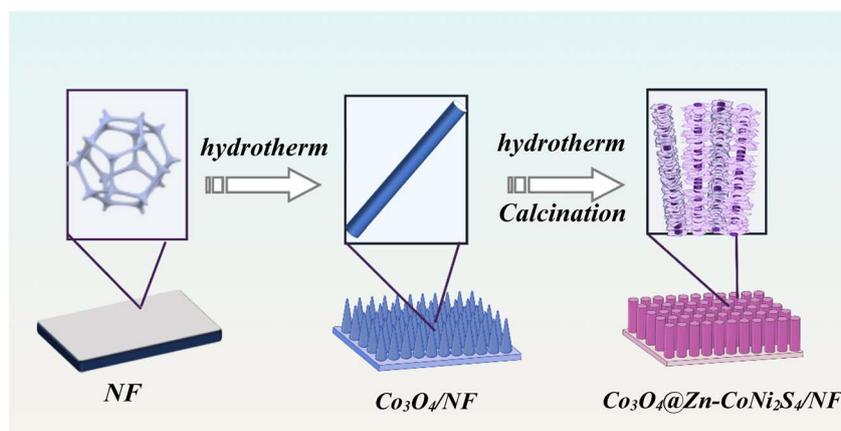

Fig. 1 Schematic diagram of the synthesis of Co$_3$O$_4$@Zn–CoNi$_2$S$_4$/NF.

of the $Co_3O_4@CoNi_2S_4$ heterostructure. In addition, EDS analysis reveals that all constituent elements in the composite are uniformly distributed, including Co, Ni, O, S, and Zn.

The XRD patterns of the as-fabricated samples are presented in Fig. 3a. First, the strong peaks located at 44.1°, 51.4°, and 75.6° are detected in all samples, which are assigned to the NF substrate (JCPDS no. 65-2865). For the final $Co_3O_4@CoNi_2S_4$/NF catalyst, distinct diffraction peaks at 31.1°, 36.8°, 38.8°, and 65.2° are indexed to the cubic Co_3O_4 phase (JCPDS no. 00-009-0418). Moreover, the additional peaks appearing at 16.2°, 33.2°, 38.12°, and 54.9° match well with the (111), (220), (311), (440), and (551) planes of $CoNi_2S_4$ (JCPDS no. 04-010-2269), confirming the successful formation of the sulfide phase. The above XRD results are consistent with the TEM-SAED and EDS analyses, collectively verifying the coexistence of the dual phases in the $Co_3O_4@CoNi_2S_4$/NF composite. Notably, a distinct shift in the XRD peaks can be clearly observed from the patterns, indicating that Zn^{2+} has been incorporated into the lattice *via* substitutional doping, with the lattice undergoing modulation.

To investigate the surface chemical states, XPS measurements are performed. As displayed in Fig. 3b, the survey spectrum of $Co_3O_4@Zn–CoNi_4S_2$/NF exhibits distinct peaks corresponding to Ni, Co, O, S, and Zn. This result confirms the coexistence of all expected elements in the final catalyst. The distinct Zn 2p signal confirms that Zn is effectively the lattice of $Co_3O_4@CoNi_2S_4$/NF at the atomic scale. High-resolution XPS

spectra are analyzed to investigate how Zn incorporation affects the surface electronic structure. By comparing the Co 2p spectra before and after doping (Fig. 3c), distinct changes can be observed. The $Co_3O_4@CoNi_2S_4$/NF sample displays typical spin–orbit doublets, corresponding to the $2p_{3/2}$ and $2p_{1/2}$ states. The peak pairs with binding energies of 780.8 eV and 796.7 eV indicate the presence of the Co^{3+} oxidation state in the sample. Meanwhile, the peak pairs at 781.4 eV and 797.5 eV matches the typical characteristic of Co^{2+}, revealing the coexistence of mixed valence states.[35] The satellite peak of $2p_{3/2}$ is located at 800.0 eV, reflecting the presence of unsaturated coordination or defect structures on the material surface. After Zn doping into $Co_3O_4@CoNi_2S_4$/NF, the introduction of Zn^{2+} the local coordination environment of Co. To maintain charge balance, partial Co^{2+} is induced to convert to Co^{3+}, leading to an increase in the oxidation state of Co. The abundant presence of Co^{3+}, which has stronger oxidizing ability, promotes charge transfer and optimizes reaction pathways.[36] In Fig. 3d, the peaks at 854.8 eV and 872.8 eV confirm that Ni in the sample mainly exists in the divalent state. Associated with the Ni^{3+} state are the binding energies located at 856.4 eV and 874.5 eV. In the meantime, high-intensity satellite peaks are found at 879.3 eV and 861 eV. Zn doping leads to a slight positive shift in the binding energies of Ni^{2+}, which move from 854.8 eV and 872.8 eV to 855.2 eV and 873.2 eV. Additionally, Zn doping triggers the oxidation of Ni^{2+} to Ni^{3+}, resulting in a positive shift of the Ni^{3+} main peaks from
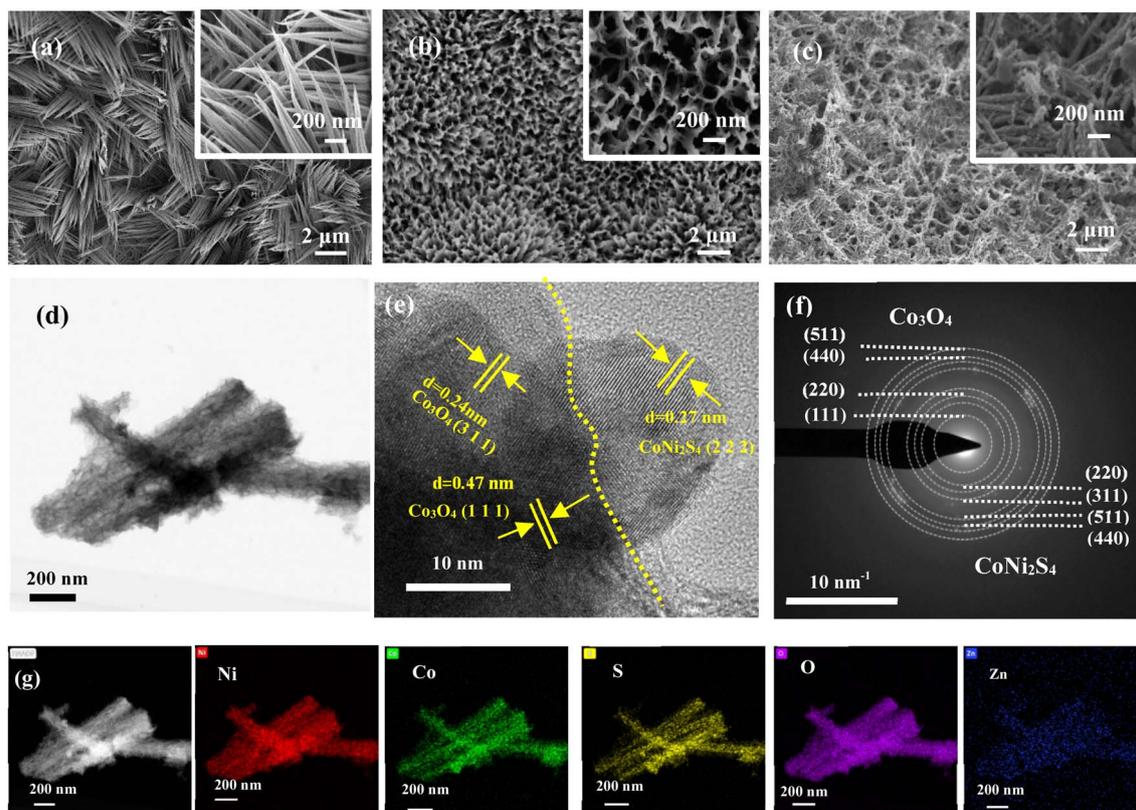

Fig. 2 (a) SEM images of Co_3O_4/NF; (b) SEM images of $Co_3O_4@CoNi_2S_4$/NF; (c) SEM images of $Co_3O_4@Zn–CoNi_2S_4$/NF; (d) TEM images of $Co_3O_4@Zn–CoNi_2S_4$; (e) HRTEM of $Co_3O_4@Zn–CoNi_2S_4$; (f) SAED of $Co_3O_4@Zn–CoNi_2S_4$; (g) EDS of $Co_3O_4@Zn–CoNi_2S_4$.
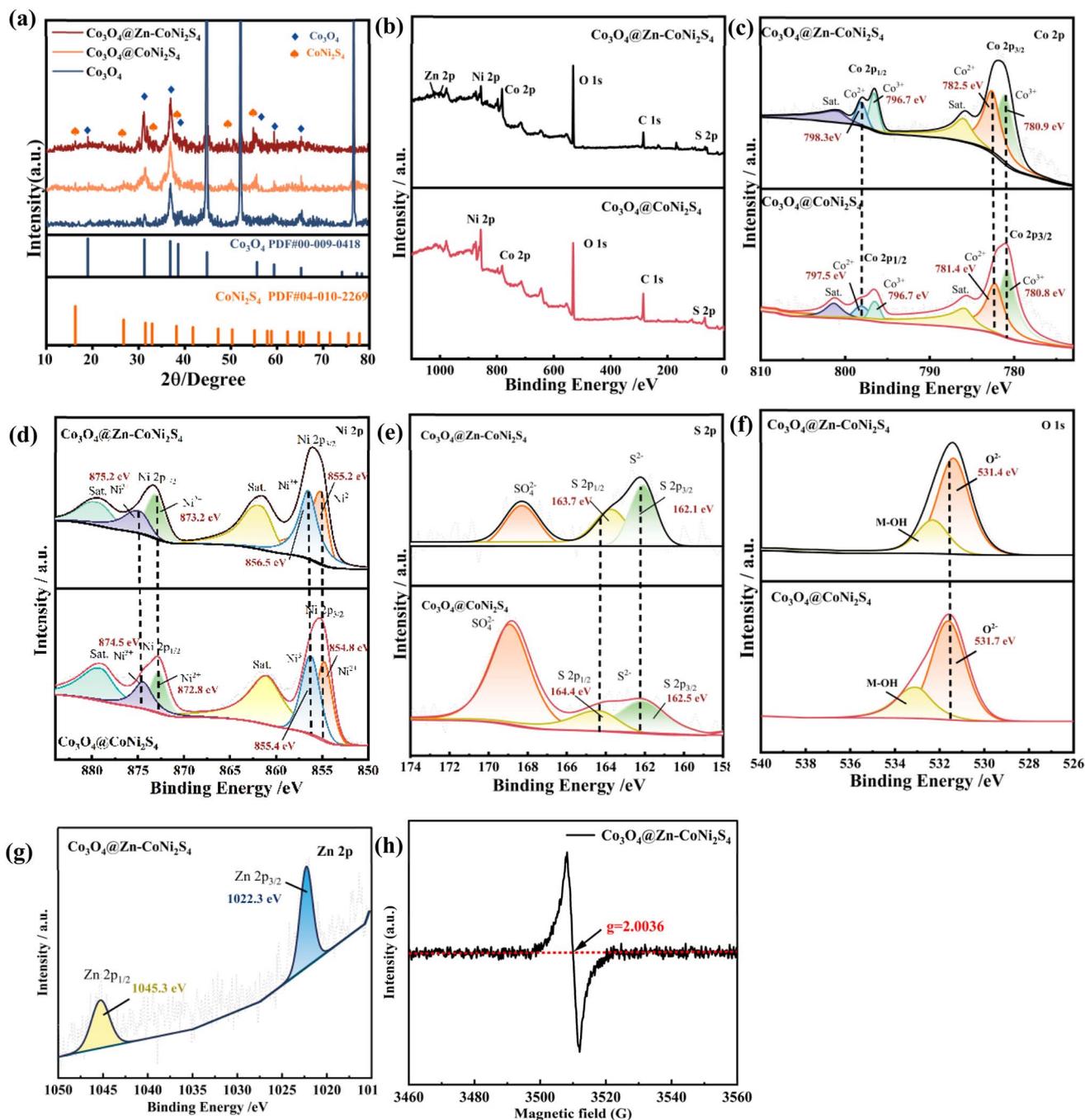
Fig. 3 (a) XRD pattern of the Co_3O_4, $Co_3O_4@CoNi_2S_4$ and $Co_3O_4@Zn-CoNi_2S_4$; (b) wide scan XPS spectrum; (c–g) high-resolution XPS spectra of Co 2p, Ni 2p, S 2p, O 1s and Zn 2p for $Co_3O_4@CoNi_2S_4$ and $Co_3O_4@Zn-CoNi_2S_4$. (h) EPR spectra of the samples $Co_3O_4@Zn-CoNi_2S_4$.

856.4 eV and 874.5 eV to 856.5 eV and 875.2 eV; the satellite peaks also exhibit a positive shift, changing from 879.3 eV to 879.6 eV. Since the electronegativity of Zn is lower than that of Co and Ni, Zn substitution for Co/Ni sites after doping requires the oxidation of adjacent Ni^{2+} to Ni^{3+} to maintain charge balance, leading to an increase in the binding energy of Ni main peaks.[37,38] in Fig. 3e, the S 2p binding energies of $Co_3O_4@Zn-CoNi_2S_4$/NF are slightly lower than $Co_3O_4@CoNi_2S_4$/NF. the characteristic peaks shift from 162.5 eV and 164.4 eV to 162.1 eV and 163.7 eV, respectively. After Zn^{2+} doping, charge transfer

occurs from the 3d orbital of Zn to the 3p orbital of S.[39,40] This transfer increases the valence electron density of S. It also weakens the adsorption of *OH. As a result, OER performance is enhanced. For Fig. 3f, the O 1s peaks of $Co_3O_4@CoNi_2S_4$/NF are located at 531.7 eV and 533.1 eV. In contrast, those of $Co_3O_4@Zn-CoNi_2S_4$/NF are at 531.4 eV and 532.4 eV. Compared with the undoped sample, there are notable changes in surface-adsorbed species and subtle modifications to the overall electronic structure. Meanwhile, this observation indicates that the material itself maintains a stable oxidation state. In the O 1s

spectrum, the peak located at 531.4 eV is correlated with oxygen vacancies. For the Zn-doped sample, this peak exhibits a higher intensity and a negative shift of 0.3 eV. The generation of abundant surface oxygen vacancies is indicated by this result, and these vacancies can facilitate the adsorption of *OH intermediates.[41] As shown in the Fig. 3g, a clear doublet corresponding to Zn $2p_{3/2}$ and Zn $2p_{1/2}$ can now be observed at binding energies of approximately 1022.3 eV and 1045.3 eV, respectively. These values are confirming the successful incorporation of Zn into the $CoNi_2S_4$ lattice. As shown in Fig. 3h, a distinct EPR signal with a g-value of 2.0036 is observed at room temperature. This g-value is close to that of a free electron (2.0023), which is a typical characteristic of unpaired electrons associated with oxygen vacancies in metal oxides. The slight deviation may originate from spin–orbit coupling and the local electronic environment surrounding the defect sites. The emergence of this strong EPR signal confirms that a large number of oxygen vacancies are successfully introduced into the $Co_3O_4@Zn–CoNi_2S_4$/NF structure.

3.2 Electrochemical measurements

As can be seen from the figure, with the increase of $CoNi_2S_4$ loading, the electrocatalytic activity of the samples first increased and then decreased in Fig. S3a and b. When the total concentration of Co^{2+} and Ni^{2+} was 50 mmol L^{-1} (corresponding to the C-50 sample), the electrocatalytic performance reached the optimal level; when the total concentration of metal ions further increased, excessive $CoNi_2S_4$ loading led to the collapse of the pore structure, which in turn reduced the contact area between the electrode and the electrolyte as well as the electron transfer efficiency, resulting in a significant attenuation of electrocatalytic performance.

To further investigate the regulatory role of Zn introduction, a series of $Co_3O_4@Zn–CoNi_2S_4$/NF composites were synthesized with varying Zn^{2+} doping levels ($x = 1, 3, 5,$ and 6 at%) in Fig. S3c and d. Electrochemical evaluations revealed that the catalytic activity followed a trend dependent on the doping concentration, with the optimal performance achieved at 3 at% Zn. This enhancement is attributed to the synergistic effects of Zn-induced lattice defects, the modulation of the electronic structure, and optimized interfacial interactions. With the optimal synthesis parameters established, the electrochemical activity of the resultant $Co_3O_4@Zn–CoNi_2S_4$/NF was systematically evaluated in a three-electrode system.

The OER performance is evaluated in a three-electrode system. As shown in the LSV curves (Fig. 4a), $Co_3O_4@Zn–CoNi_2S_4$/NF exhibits the lowest overpotential among all samples. Specifically, the catalyst delivers 10 and 100 mA cm^{-2} at overpotentials of merely 190 and 313 mV in Fig. 4b. This result underscores the superior activity of the Zn-doped core–shell architecture, which can be traced back to the favorable synergistic interactions. The highly conductive outer shell serves as a conduit for rapid interfacial electron transfer, effectively mitigating the redox overpotential. Concurrently, lattice expansion triggered by Zn doping further amplifies the intrinsic electrocatalytic activity. Reaction kinetics are

elucidated via Tafel plots (Fig. 4c), where a lower slope typically serves as a hallmark of reduced charge transfer resistance. Notably, $Co_3O_4@Zn–CoNi_2S_4$/NF demonstrates a superior Tafel slope of 47.2 mV dec^{-1}, significantly outperforming both $Co_3O_4@CoNi_2S_4$/NF (46.94 mV dec^{-1}) and pristine Co_3O_4/NF (116.4 mV dec^{-1}). This result confirms that $Co_3O_4@Zn–CoNi_2S_4$/NF shows the optimal electrochemical reaction kinetics. The incorporation of Zn adjusts the electronic structure of Ni^{3+} and creates abundant oxygen vacancies. These factors work together to lower the energy barrier, leading to faster charge transfer. The fitting of EIS tests is performed under open-circuit potential in Fig. 4d, the $Co_3O_4@Zn–CoNi_2S_4$/NF sample possesses the smallest charge transfer resistance (R_{ct}) of 2.7 Ω, offering direct proof of its enhanced conductivity. To determine the electrochemical active surface area, C_{dl} is calculated from the non-faradaic region (Fig. 4e). The $Co_3O_4@Zn–CoNi_2S_4$/NF sample records the high C_{dl}, signifying a larger active surface area and a greater number of exposed active sites for OER. Stability is equally crucial as catalytic activity. As shown in Fig. 4f, the durability was tested using chronopotentiometry at l0 mA cm^{-2}, the potential remained stable at roughly l90 mV for 20 h without significant fluctuation, proving its excellent long-term stability.

After the cyclic stability test, comprehensive characterization by HRTEM, Raman and XPS spectroscopy, and revealed a significant surface reconstruction of the material, elucidating the structural and chemical evolution underlying its electrocatalytic activity. The HRTEM image of the post-OER sample in Fig. S8 reveals a well-defined core–shell heterostructure. The crystalline core retains distinct lattice fringes corresponding to the $CoNi_2S_4$ and Co_3O_4 phases, confirming the preservation of long-range order and structural robustness. In contrast, the surface is encapsulated by an outer layer, consistent with the characteristics of oxyhydroxide formation. This reconstructed shell provides abundant coordinatively unsaturated sites favorable for OER catalysis, while the intact crystalline core ensures efficient electron transport. In Fig. S9, Raman spectroscopy results further corroborate these findings. Before cycling, the characteristic peaks located at 300 cm^{-1} and 350 cm^{-1} are attributed to the lattice vibrations of metal–sulfur (M–S) bonds, while the peaks at 526 cm^{-1} and 669 cm^{-1} correspond to Co_3O_4, verifying the composite nature of the pristine material. After electrocatalytic cycling, the vibrational modes of M–S bonds nearly vanish, indicating the complete oxidation of surface sulfur species. Concomitantly, a new broad and intense peak appears at 552 cm^{-1}, which is assigned to the metal oxyhydroxide (M–OOH) phase, further confirming the formation of a surface oxyhydroxide layer.

The XPS analysis reveals significant alterations in the electronic structure and chemical valence states of surface elements. As shown in Fig. 7b and c, the Co 2p and Ni 2p spectral peaks shift toward higher binding energies, accompanied by a significant increase in the relative proportions of trivalent cobalt (Co^{3+}) and trivalent nickel (Ni^{3+}). The generation of these high-valence metal states indicates the formation of more electrophilic active centers during the electrochemical reconstruction. Such electron-deficient sites are theoretically
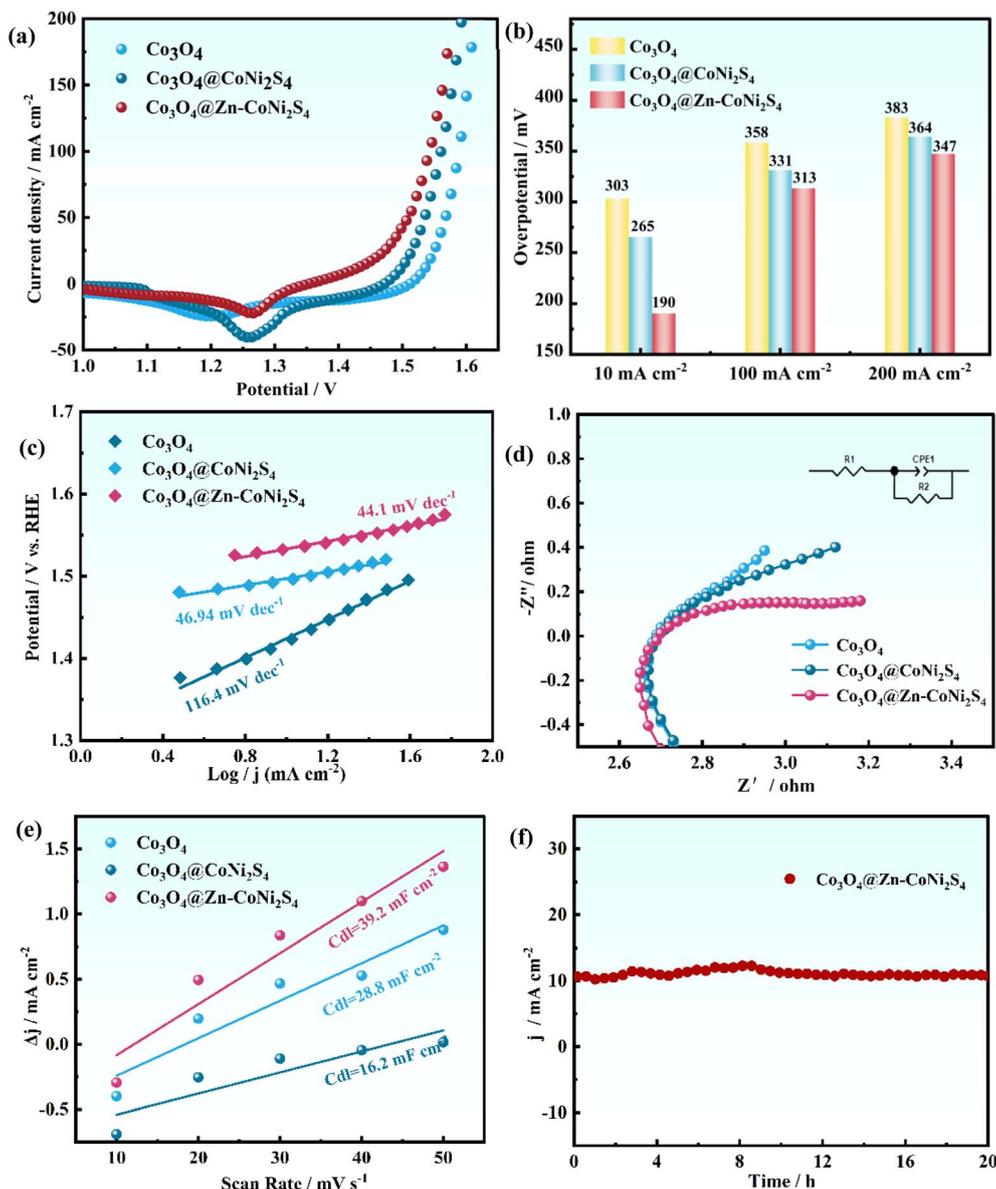
Fig. 4 Electrocatalytic performance evaluation for OER. (a) LSV curve in 1.0 M KOH. (b) Comparison of overpotential. (c) Tafel plots. (d) EIS spectra. (e) C_{dl} calculations. (f) Chronopotentiometry curves at 10 mA cm^{-2}.

favorable for facilitating the adsorption and deprotonation of oxygenated intermediates, which substantially lowers the kinetic energy barrier and boosts the overall OER performance. Concurrently, as depicted in Fig. 5d, the S 2p signal intensity decreases drastically. This surface desulfurization process exposes more accessible metal active centers, representing a critical activation step. In the O 1s spectrum (Fig. 5e), the intensity of the metal–hydroxyl (M–OH) characteristic peak at 531.5 eV increases significantly after cycling, while the intensities of lattice oxygen (M–O) and adsorbed water remain relatively stable, providing strong evidence for the formation of a hydroxyl-rich oxyhydroxide layer. Furthermore, the decrease in Zn content post-cycling indicates partial zinc leaching, a process that likely induces the generation of surface vacancies, thereby further enhancing the accessibility of active sites;

if zinc is retained, its role in stabilizing the bulk framework structure should be emphasized (Fig. 5f).

In summary, the post-characterization results confirm that Co$_3$O$_4$@Zn–CoNi$_2$S$_4$ acts as a pre-catalyst. Under OER conditions, it undergoes surface reconstruction to form a CoOOH/NiOOH active shell supported on a conductive Co$_3$O$_4$/CoNi$_2$S$_4$ core. This unique architecture combines abundant active sites with efficient electron transport channels, leading to superior electrocatalytic performance.

In the HER tests, LSV performances of three samples (Co$_3$O$_4$@Zn–CoNi$_2$S$_4$/NF, Co$_3$O$_4$@CoNi$_2$S$_4$/NF, and Co$_3$O$_4$/NF) are compared. As presented in Fig. 6a, the overpotentials required to reach a current density of 10 mA cm^{-2} are 120 mV, 159 mV, and 168 mV for Co$_3$O$_4$@Zn–CoNi$_2$S$_4$/NF, Co$_3$O$_4$@-CoNi$_2$S$_4$/NF, and Co$_3$O$_4$/NF, respectively. The Pt/C catalyst is
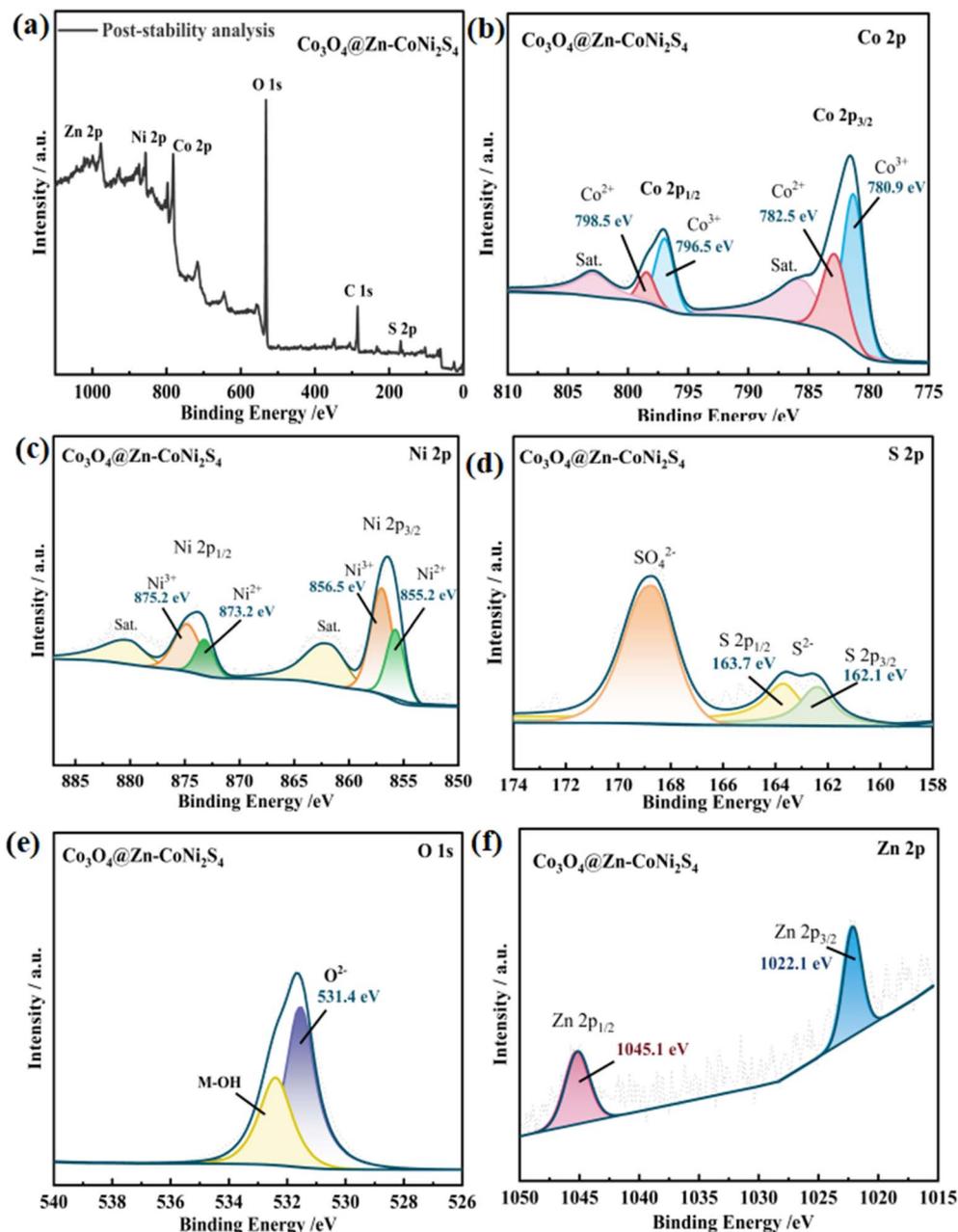
Fig. 5 The post-OER XPS spectra (a) wide scan XPS spectrum; (b–f) high-resolution XPS spectra of Co 2p, Ni 2p, S 2p, O 1s and Zn 2p for $Co_3O_4@Zn-CoNi_2S_4$.

only 42.4 mV under the same conditions. This confirms that Pt/ C possesses outstanding activity as a benchmark catalyst for HER. Although there is a performance gap between our sample and Pt/C, the performance of our sample is superior to that of many other non-noble metal materials compared, which highlights its potential application value. This indicates that the electrocatalytic performances of the $Co_3O_4@Zn-CoNi_2S_4$/NF sample are significantly enhanced. Fig. 6b illustrates the overpotentials of the catalysts at current densities of 10 mA cm^{-2}, 100 mA cm^{-2}, and 200 mA cm^{-2}. The enhanced HER activity of $Co_3O_4@Zn-CoNi_2S_4$/NF originates from the synergistic effect between the constructed core–shell heterostructure and Zn

doping. To gain insights into HER kinetics, Tafel slope analysis was performed to further elucidate the reaction mechanism on the catalyst surface. As presented in Fig. 6c, the Tafel slopes of $Co_3O_4@Zn-CoNi_2S_4$/NF, $Co_3O_4@CoNi_2S_4$/NF, and Co_3O_4/NF are 46.3, 51.2, and 68.54 mV dec^{-1}. Mechanistically, the interfacial structure of $Co_3O_4@CoNi_2S_4$/NF appears to drive electron transfer primarily through the Heyrovsky pathway. However, the incorporation of Zn introduces a pivotal kinetic modulation, accelerating the recombination and desorption processes characteristic of the Tafel step. Since the Tafel mechanism typically offers a more energetically favorable route for molecular evolution compared to electrochemical desorption, this Zn-
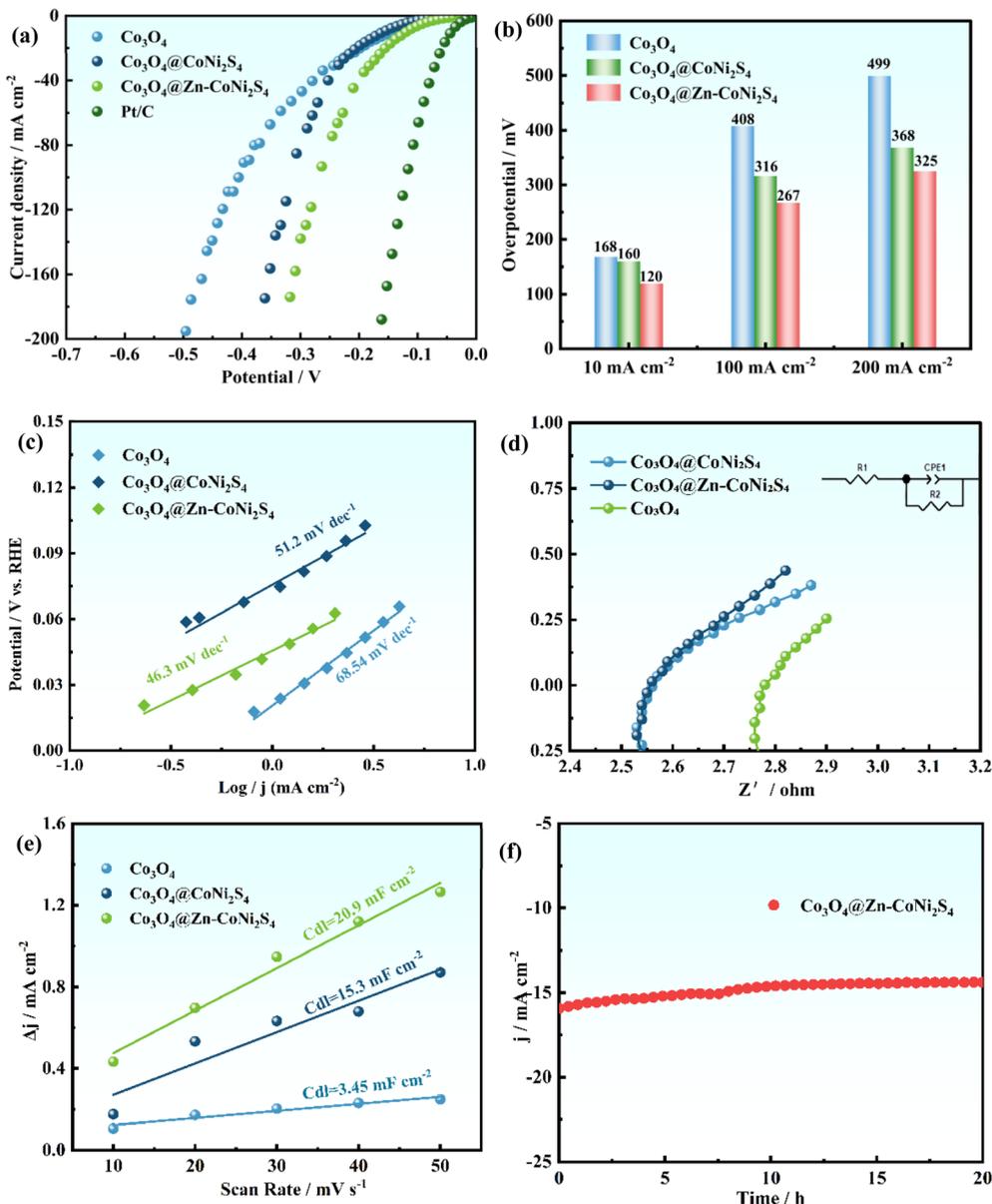
Fig. 6 Electrocatalytic performance evaluation for HER. (a) LSV curve in 1.0 M KOH. (b) Comparison of overpotential. (c) Tafel plots. (d) EIS spectra. (e) C_{dl} calculations. (f) Chronopotentiometry curves at 10 mA cm^{-2}.

induced shift plays a decisive role in maximizing the overall efficiency of hydrogen production. Fig. 6d shows the open-circuit voltage fitting plot obtained during the HER electro-catalytic test. Co$_3$O$_4$@Zn–CoNi$_2$S$_4$/NF exhibits a smaller R_{ct} (2.55 Ω) compared to Co$_3$O$_4$@CoNi$_2$S$_4$/NF (2.56 Ω) and Co$_3$O$_4$/ NF (2.78 Ω). This indicates that the introduction of the CoNi$_2$S$_4$ shell constructs a high-speed electron transport channel at the heterogeneous interface, reducing the interfacial electric field gradient, while Zn doping further fine-tunes the surface electronic structure. Meanwhile, the expansion of the specific surface area synchronously increases the number of intrinsic active sites per unit geometric area, thereby enhancing the HER kinetics. Analysis of Fig. 6e shows the C_{dl} values,20.9 mF cm^{-2} for Co$_3$O$_4$@Zn–CoNi$_2$S$_4$/NF, 15.3 mF cm^{-2} for Co$_3$O$_4$@CoNi$_2$S$_4$/

NF and 3.45 mF cm^{-2} for Co$_3$O$_4$/NF. Co$_3$O$_4$@Zn–CoNi$_2$S$_4$/NF outperforms the other two samples mainly because the heterostructure in Co$_3$O$_4$@CoNi$_2$S$_4$/NF forms a porous network, which increases the specific surface area and exposes more active sites. Cycling stability tests of Co$_3$O$_4$@Zn–CoNi$_2$S$_4$/NF are performed at a constant current density of −10 mA cm^{-2} for 20 h (Fig. 6f). The voltage fluctuation is less than 5%, indicating excellent long-term stability. Furthermore, the influence of electrolyte pH on the catalytic activity is investigated, and the results confirm that the as-prepared catalyst delivers superior performance specifically in alkaline environments, validating its suitability for alkaline water splitting applications as shown in Fig. S4.
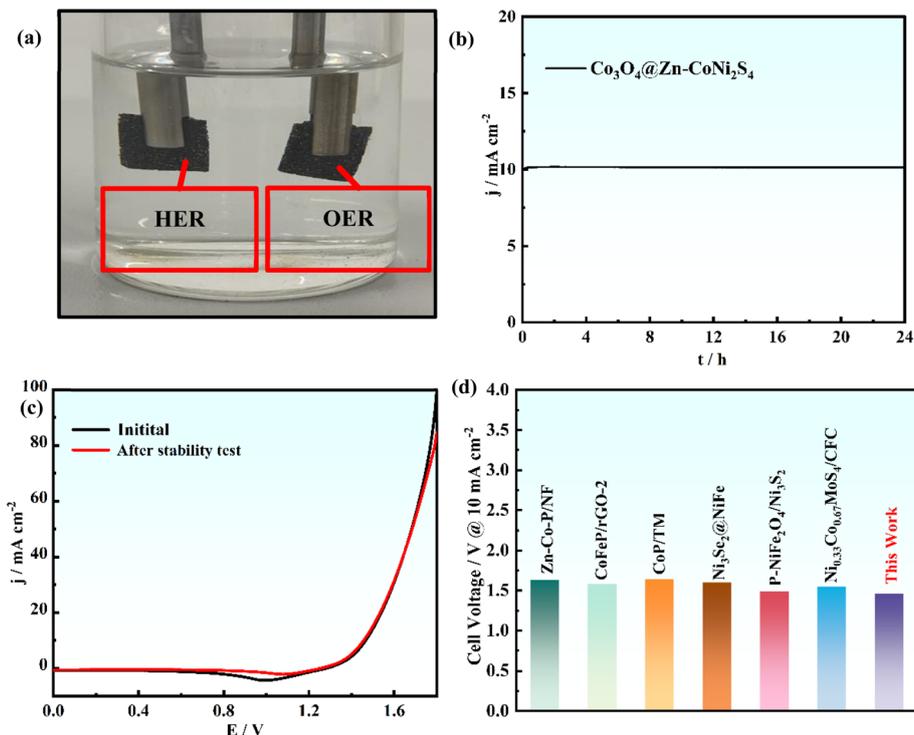
Fig. 7 Overall water splitting performance in a two-electrode electrolyzer. (a) Photograph of gas evolution. (b) Chronoamperometry stability test. (c) LSV curves before and after stability test; (d) performance compared to other non-precious metal-based electrocatalysts (the cell voltage at 10 mA cm^{-2}).

Motivated by its outstanding performance in both OER and HER, a two-electrode electrolyzer was constructed employing Co_3O_4@Zn–$CoNi_2S_4$/NF as the bifunctional catalyst for both the anode and cathode (Fig. 7a). As shown in Fig. 7b, this system requires a cell voltage of only 1.45 V to drive a current density of 10 mA cm^{-2}. To verify its durability, the LSV curve is recorded again after 20 hours of continuous operation. As displayed in Fig. 7c, the curve overlaps well with the initial one, indicating negligible degradation. Furthermore, this performance is superior to the most reported catalysts listed in Fig. 7d.[42–48] To evaluate the catalytic efficiency, FE measurements are performed in a two-electrode system using Co_3O_4@Zn–$CoNi_2S_4$/NF as both anode and cathode, with H_2 and O_2 collected separately through water displacement. The molar ratio of H_2 to O_2 is found to be nearly 2 : 1, confirming the high FE and authenticity of the overall water splitting performance in the Fig. S7.

4 Conclusion

This study presents a low-cost, self-supported Co_3O_4@Zn–$CoNi_2S_4$/NF electrode with a core–shell heterostructure. The synergistic effect of Zn doping and heterointerfaces effectively modulates the electronic structure, creates abundant active sites, and thereby endows the material with remarkable bifunctional catalytic activity in alkaline media. The electrode requires low overpotentials of only 190 mV for OER and 120 mV for HER to achieve 10 mA cm^{-2}, alongside excellent stability. An electrolyzer assembled with this electrode delivers the same current density at a low cell voltage of 1.45 V for overall water

splitting. This work provides a viable strategy for designing efficient electrocatalysts through interfacial engineering.

Author contributions

Xuan Zhao: writing original draft; methodology. Yu Dong: validation; data curation. Zhijie Wang and Yusheng Qiu: investigation visualization and resources. Ende Wang: supervision; project administration. Naikun Sun: conceptualization; funding acquisition. Yongli Tong: supervision; funding acquisition.

Conflicts of interest

There are no conflicts to declare.

Data availability

The data that support the findings of this study are available from the corresponding author upon reasonable request.

Supplementary information (SI): detailed experimental procedures, additional characterization data, and electrochemical performance curves. See DOI: https://doi.org/10.1039/d5ra09427e.

Acknowledgements

References

1 S. Ahmad, A. Ullah, A. Samreen, M. Qasim, K. Nawaz, W. Ahmad, A. Alnaser, A. M. Kannan and M. Egilmez, *J. Energy Storage*, 2024, **101**, 113733.

2 I. Dincer and M. I. Aydin, *Energy Convers. Manage.*, 2023, **283**, 116950.

3 V. Beschkov and E. Ganev, *Energies*, 2023, **16**, 6108.

4 R. Mulla and C. W. Dunnill, *Energy Earth Sci.*, 2020, **3**, 49.

5 S.-L. Zheng, H.-M. Xu, H.-R. Zhu, T.-Y. Shuai, Q.-N. Zhan, C.-J. Huang and G.-R. Li, *J. Mater. Chem. A*, 2024, **12**, 18832–18865.

6 P. Wang, Y. Lin, L. Wan and B. Wang, *Energy Fuels*, 2020, **34**, 10276–10281.

7 Y. Wu, X. Du and X. Zhang, *J. Alloys Compd.*, 2025, **1030**, 180927.

8 X. Liu, W. Zhang, X. Wu and Y.-R. Cho, *Energy Mater. Adv.*, 2025, **6**, 0160.

9 H. Wang, K. H. L. Zhang, J. P. Hofmann, V. A. de la Peña O'Shea and F. E. Oropeza, *J. Mater. Chem. A*, 2021, **9**, 19465–19488.

10 P. S. Venkatesh, N. Kannan, M. G. Babu, G. Paulraj and K. Jeganathan, *Int. J. Hydrogen Energy*, 2022, **47**, 37256–37263.

11 X. Yu, X. Wang, S. Wu, J. Bai, P. He, F. Qin, Y. Yao and L. Ren, *J. Alloys Compd.*, 2023, **946**, 169383.

12 A. I. Inamdar, A. S. Salunke, J. H. Seok, H. S. Chavan, N. K. Shrestha, S. U. Lee, S. Cho and H. Im, *J. Mater. Chem. A*, 2024, **12**, 31362–31374.

13 C. He, L. Yang, J. Wang, T. Wang, J. Ju, Y. Lu and W. Chen, *Carbon Energy*, 2024, **6**, e573.

14 Y. Feng, J. Jia, Z. Zou, Y. Lin, X. Zheng, W. Lai, X. Chen, Q. Wang and C. Xu, *Chem. Eng. J.*, 2025, **520**, 166004.

15 G. Mustafa, M. Saleem, I. Ahmad, M. Sohail, S. H. Gillani, M. F. Nazar, R. Zairov, A. Syed, A. M. Elgorban and A. H. Bahkali, *Emergent Mater.*, 2025, **8**, 4187–4195.

16 L. Zan, H. Zhang, X. Bo, Y. Zhao, H. Tian, H. Chen, Q. Wei, H. Tang and F. Fu, *J. Alloys Compd.*, 2021, **869**, 159324.

17 B. Tian, P. Cheah, J. Qu, F. Han, X. Zhu and Y. Zhao, *Mater. Today Energy*, 2024, **40**, 101494.

18 T. Yang, H. Xie, N. Ma, E. Liu, C. Shi, C. He and N. Zhao, *Appl. Surf. Sci.*, 2021, **550**, 149355.

19 Z. Guo, G. Tian, L. Liu, B. Zhang, Q. Wu, Y. Cao, J. Tu, L. Ding and X. Zhang, *J. Mater. Sci. Technol.*, 2021, **89**, 52–58.

20 A. Q. Mugheri, A. Tahira, U. Aftab, M. I. Abro, S. R. Chaudhry, L. Amaral and Z. H. Ibupoto, *Electrochim. Acta*, 2019, **306**, 9–17.

21 Y.-L. Tong, L. Xing, M.-Z. Dai and X. Wu, *Front. Mater.*, 2019, **6**, 6.

22 T. Liu, J. Guo, A. Wu, Y. Fan, Y. Xie and C. Tian, *ACS Appl. Nano Mater.*, 2024, **7**, 13298–13307.

23 W. Dai, K. Ren, Y.-A. Zhu, Y. Pan, J. Yu and T. Lu, *J. Alloys Compd.*, 2020, **840**, 156252.

24 Y. Wu, L. Su, Q. Wang and S. Ren, *Ionics*, 2022, **28**, 4935–4942.

25 G. Du, Y. Fan, L. Jia, Y. Wang, Y. Hao, W. Zhao, Q. Su and B. Xu, *Front. Chem. Sci. Eng.*, 2023, **17**, 1750–1759.

26 L. Zheng, S. Wang, Y. Wang, Z. Zhao, P. Yang, J. Song, X. Shi and H. Zheng, *Nanotechnology*, 2022.

27 J. Tang, K. Ren, Y. Zhang, W. Shen, R. He and M. Li, *J. Phys. Chem. C*, 2021, **125**, 10140–10150.

28 M. Wang, X. Liu and X. Wu, *Nano Energy*, 2023, **114**, 108681.

29 H. Qian, N. Huang, J. Zheng, Z. An, X. Yin, Y. Liu, W. Yang and Y. Chen, *J. Colloid Interface Sci.*, 2021, **598**, 83–93.

30 B. J. Rani, G. Ravi, R. Yuvakkumar, S. Ravichandran, F. Ameen and A. Al-Sabri, *J. Sol-Gel Sci. Technol.*, 2018, **87**, 713–723.

31 L. S. Graves, R. Sarkar, K. U. Lao and I. U. Arachchige, *Chem. Mater.*, 2023, **35**, 7181–7191.

32 Y. Lin, X. Cui, Y. Zhao, Z. Liu, G. Zhang and Y. Pan, *Nano Res.*, 2023, **16**, 8765–8772.

33 Y. Wang, S. Liu, X. Du and X. Zhang, *Int. J. Hydrogen Energy*, 2024, **88**, 450–461.

34 Y. Lin, Y. Pan, S. Liu, K. Sun, Y. Cheng, M. Liu, Z. Wang, X. Li and J. Zhang, *Appl. Catal., B*, 2019, **258**, 118039.

35 R.-P. Wang, M.-J. Huang, A. Hariki, J. Okamoto, H.-Y. Huang, A. Singh, D.-J. Huang, P. Nagel, S. Schuppler, T. Haarman, B. Liu and F. M. F. de Groot, *J. Phys. Chem. C*, 2022, **126**, 8752–8759.

36 C. Wang, Q. Geng, L. Fan, J.-X. Li, L. Ma and C. Li, *Nano Res. Energy*, 2023, **2**, e9120070.

37 M. K. Gurjar, T. Harsh, R. Dash and A. S. Bhattacharyya, *MRS Adv.*, 2023, **8**, 925–930.

38 T. Sen, A. Biswas, T. K. Rout, R. Thangavel and U. G. Nair, *J. Alloys Compd.*, 2021, **889**, 161613.

39 Y. Wu, X. Du and X. Zhang, *Int. J. Hydrogen Energy*, 2025, **103**, 174–182.

40 L. Zhao, K. Meng, Y. Guo, Q. Wu, Q. Zhu, T. Zhou, Y. Fu and M. Wen, *Nano Res. Energy*, 2024, **3**, e9120129.

41 Y. Yang, X. Wang, G. Yi, H. Li, C. Shi, G. Sun and Z. Zhang, *Nanomaterials*, 2019, **9**, 1599.

42 S. Kumaravel, B. Avula, C. Chandrasatheesh, T. Niyitanga, R. Saranya, I. Hasan, T. Abisheik, R. S. Rai, V. Pandiyan and K. Balu, *Spectrochim. Acta, Part A*, 2024, **310**, 123972.

43 L. Zhang, L. Li, J. Liang, X. Fan, X. He, J. Chen, J. Li, Z. Li, Z. Cai, S. Sun, D. Zheng, Y. Luo, H. Yan, Q. Liu, A. A. Alshehri, X. Guo, X. Sun and B. Ying, *Inorg. Chem. Front.*, 2023, **10**, 2766–2775.

44 Y. Song, Q. Wang, X. Liu, C. Zhou, S. Li, S. Wang, Y. Sun and P. Zhang, *Catal. Lett.*, 2024, **154**, 5101–5109.

45 R. Fu, Q. Jiao, C. Yang, X. Jiao, X. Zhang, C. Feng, H. Li, Y. Zhang and Y. Zhao, *New J. Chem.*, 2023, **47**, 1226–1233.

46 B. Du, J. Zhao, L. Tian, Q. Wang, X. Ren, X. Sun, Q. Wei, Y. Li and D. Wu, *New J. Chem.*, 2022, **46**, 13117–13121.

47 J. Wang, Y. Dong, X. Zheng, B. Long, H. Ling, L. Xie, Z. Xiang and W. He, *Appl. Surf. Sci.*, 2025, **694**, 162834.

48 J. Hu, S. Zhu, Y. Liang, S. Wu, Z. Li, S. Luo and Z. Cui, *J. Colloid Interface Sci.*, 2021, **587**, 79–89.